



Effective Role of Two Layers of Silica in the Performance of $\text{Fe}_3\text{O}_4@x\text{SiO}_2@y\text{SiO}_2@\text{BisPyP-Ni}$ Core-Shell Catalyst for C-C and C-S Coupling Reactions

Ebraheem Abdu Musad Saleh¹ · Asmaa F. Kassem^{1,2} · Farag M. A. Altalbawy^{3,4} · Sarah Jawad Shoja⁵ · Dmitry Olegovich Bokov^{6,7} · Ahmed Elawady^{9,10,8} · Ameer H. Al-Rubaye¹¹ · Abdunaser Saud¹² · Zuhair I. Al-Mashhadani¹³ · Maryam Sadat Ghorayshi Nejad¹⁴

Received: 1 January 2024 / Accepted: 21 March 2024

© The Author(s), under exclusive licence to Springer Nature B.V. 2024

Abstract

In this research, a novel core-shell nanocatalyst with silica bi-shell around Fe_3O_4 and nickel active center, i.e. $\text{Fe}_3\text{O}_4@x\text{SiO}_2@y\text{SiO}_2@\text{BisPyP-Ni}$ was synthesized and its characteristics were comprehensively discussed. This nanocatalyst was successfully used to synthesize biaryls (18 examples, 15–30 min, 92–98%) and diaryl sulfides (10 examples, 20–140 min, 79–98%) at 80 °C. Excellent performance in speeding up the reaction time, magnetic nature, high porosity, and immobilization of two layers around Fe_3O_4 are four prominent characteristics of this catalyst. Coating the magnetic core with silica layers led to saving the consumption of the catalyst because this trick leads to the bonding of more organic groups to the substrate, as a result, more nickel enters the mesoporous cavities, and the reaction with a smaller amount of catalyst is finished (in a shorter time). Other advantages of both our production lines are: the ability to recover and reuse the catalyst for up to 8 runs (without a noticeable decrease in its catalytic performance), extensive substrate scope, the employ of commercially accessible materials, simple workup, environmental safety and the heterogeneous nature of the catalyst (by confirming the reusability and hot filtration test results).

Keywords Silica · Core-shell catalyst · Magnetite nanoparticles · Biaryls · Di-aryl sulfides

1 Introduction

In recent years, the field of catalysis has witnessed a remarkable breakthrough with the emergence of magnetic nanocatalysts [1, 2]. Magnetic catalysts play a significant role in various chemical and industrial processes [1–3]. One of the significant benefits of magnetic catalysts is their ability to be easily separated and recovered from reaction mixtures using magnetic fields [4]. This avoids the need for time-consuming and costly traditional separation techniques, such as filtration or centrifugation [5, 6]. Magnetic separation simplifies the purification process, making it more efficient and environmentally friendly [7, 8]. Also, magnetic catalysts can significantly enhance the reactivity of chemical reactions by facilitating efficient and controlled mass transfer and accelerating reaction rates [4]. They provide a platform for more precise control and utilization of reactants, leading to

enhanced product yields and reduced reaction times [9]. The utilization of magnetic catalysts has the potential to revolutionize chemical processes, making them more efficient, sustainable, and economically viable [4, 9]. By harnessing the power of magnets, these catalysts contribute to advancements in diverse fields, from pharmaceuticals and chemicals to energy production and environmental remediation [10, 11]. In many magnetic catalysts, there is a core-shell structure. Using core-shell structures in catalyst synthesis offers a promising approach for developing highly efficient and stable catalysts with tailored properties for specific applications [10, 11]. The ability to control the thickness and composition of the shell layers allows for fine-tuning of the electronic and catalytic properties of the nanoparticles, leading to improved performance and stability [4, 9–11].

Magnetic catalysts play a significant role in coupling reactions, offering several advantages over traditional catalysts [4]. These catalysts, usually based on transition metals such as palladium, nickel, or iron, are functionalized with magnetic nanoparticles or magnetically responsive materials

Extended author information available on the last page of the article

[12]. Nickel magnetic nanocatalysts have emerged as promising alternatives to traditional palladium catalysts for coupling reactions [13]. Nickel is an abundant and less expensive metal than palladium, making nickel-based catalysts more economically viable for large-scale applications [13, 14].

Nowadays, carbon-carbon and carbon-sulfur coupling reactions have received much attention due to the various applications of their products [15, 16]. The Suzuki reaction is a powerful and widely used organic transformation that has considerable importance in synthetic chemistry [15, 16]. The Suzuki reaction allows for the formation of carbon-carbon bonds between vinyl (or aryl) boronic acids and vinyl (or aryl) halides [17]. This bond formation is critical in constructing complex organic molecules, including pharmaceuticals, agrochemicals, and materials [18, 19]. The method enables synthesizing a broad range of biaryl compounds, which are essential structural motifs found in numerous natural products and functional materials [18, 19].

Another area that has seen a significant impact is the carbon-sulfur reaction [15, 16]. Carbon-sulfur reactions provide a versatile toolkit for organic chemists to access a wide range of sulfur-containing compounds [20]. These compounds have diverse applications in pharmaceuticals, agrochemicals, materials science, and other areas [20]. The importance of carbon-sulfur reactions lies in their ability to introduce sulfur atoms into organic molecules, leading to the creation of various sulfides, sulfones, thiols, and other sulfur-containing compounds [20, 21]. C-S coupling reactions play a crucial role in the production of natural products, allowing chemists to access complex architectures and introduce key sulfur moieties present in bioactive compounds [20, 21].

One of the important products of carbon-sulfur coupling is sulfides [22, 23]. Sulfides play a crucial role in various areas of science, industry, and everyday life [22, 23]. They can participate in various chemical reactions, including oxidation, reduction, substitution, and addition reactions [24]. This versatility makes sulfides valuable in organic synthesis, and in the production of diverse industrial chemicals [25]. Sulfides can be synthesized using various sulfur-containing reagents or sulfur-transfer agents [26, 27]. One of the classical protocols for synthesizing sulfides involves using thiols as a sulfur-transfer agent [28]. Thiols have been widely utilized in the synthesis of organosulfur compounds [29]. However, they possess undesirable characteristics such as volatility, malodor, and toxicity. Considering the above points, here we reported $\text{Fe}_3\text{O}_4@\text{xSiO}_2@\text{ySiO}_2@\text{BisPyP-Ni}$ catalyst as a practical and heterogeneous catalyst for the rapid production of biphenyl and di-aryl sulfide derivatives.

2 Experimental

2.1 Apparatus and Materials

The specifications of all the raw materials and apparatus utilized are provided in the [supplementary data](#).

2.2 Preparation of $\text{Fe}_3\text{O}_4@\text{xSiO}_2@\text{ySiO}_2@\text{BisPyP-Ni}$

Bare Fe_3O_4 nanoparticles were made using the technique described in the literature [30]. To make silica-coated magnetite, 250 mL of deionized H_2O and 300 mL of ethanol were used to dilute 2.5 g of Fe_3O_4 nanoparticles. This mixture was then spread out in an ultrasonic bath for 50 min. Next, 5 mL of a concentrated ammonia aqueous solution was added to the mixture. This step took place in the presence of N_2 . Afterward, 2 mL of Tetraethylorthosilicate (TEOS) was progressively added to this dispersion and stirred at 25 °C for 10 h. This action was done with N_2 present. Subsequently, this dispersion was stirred gradually for 10 h at 25 °C while 2 mL of TEOS was added. Ultimately, a magnet was used to separate the $\text{Fe}_3\text{O}_4@\text{xSiO}_2$ nanoparticles, and they underwent several washings in distilled H_2O and EtOH before being dried at 60 °C. The generated $\text{Fe}_3\text{O}_4@\text{xSiO}_2$ (0.1 g) was dispersed in a solution containing distilled H_2O (60 mL), EtOH (40 mL), NH_4OH (25 wt%, 1 mL), and Cetyltrimethylammonium bromide (CTAB) (0.3 g) to cover the particles with nanoporous SiO_2 shells. In the following, 0.5 mL of TEOS was added to the suspension, drop by drop, and the resulting solution was agitated for 24 h at 25 °C. In continuation, the $\text{Fe}_3\text{O}_4@\text{xSiO}_2@\text{ySiO}_2$ was separated in the vicinity of the external magnetic field, and the method described in the preceding step was followed for washing and drying. To create $\text{Fe}_3\text{O}_4@\text{xSiO}_2@\text{ySiO}_2@\text{nPr-Cl}$, 2 g of $\text{Fe}_3\text{O}_4@\text{xSiO}_2@\text{ySiO}_2$ were sonicated in 60 mL of n-hexane for 35 min, then 3.5 mL 3-Chloropropyltrimethoxysilane (CPTMS) was added to the resulting solution and stirred for 24 h in toluene reflux. The magnetic nanoparticles ($\text{Fe}_3\text{O}_4@\text{xSiO}_2@\text{ySiO}_2@\text{nPr-Cl}$) were washed in ethanol, separated using an external magnet, and dried at 50 °C. The $\text{Fe}_3\text{O}_4@\text{xSiO}_2@\text{ySiO}_2@\text{nPr-Cl}$ MNPs solid (1 g) is then combined with (1 mmol) 1,3-Bis(4-pyridyl) propane in toluene (20 mL) and left to stand at 115 °C for 20 h to immobilize the BisPyP on the MNPs surface. The method's last step involved immobilizing nickel onto $\text{Fe}_3\text{O}_4@\text{xSiO}_2@\text{ySiO}_2@\text{BisPyP}$. To accomplish this, 1 g of $\text{Fe}_3\text{O}_4@\text{xSiO}_2@\text{ySiO}_2@\text{BisPyP}$ NMPs were dissolved in ethanol first, and the resultant mixture was subsequently mixed with 2 mmol of $\text{Ni}(\text{NO}_3)_2 \cdot 6\text{H}_2\text{O}$. Then, this mixture was stirred for 24 h in reflux condition. The resulting

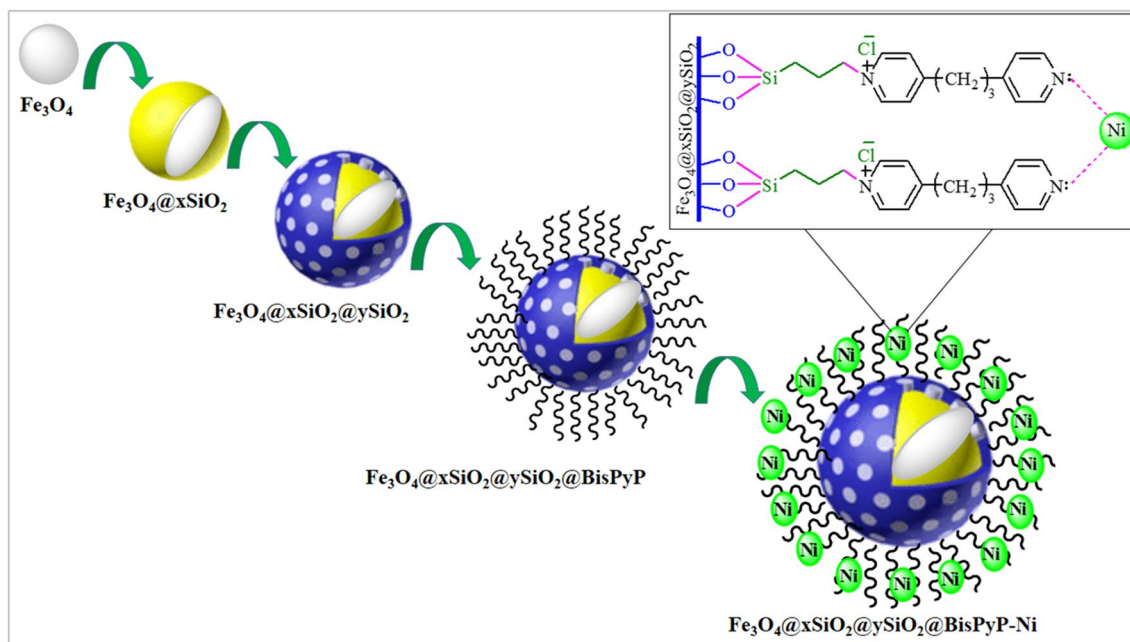
$\text{Fe}_3\text{O}_4@\text{xSiO}_2@\text{ySiO}_2@\text{BisPyP-Ni}$ NMPs were filtered and repeatedly washed with ethanol before being dried in an air environment (Scheme 1).

2.3 Typical Procedure for the Synthesis of Biaryls

In PEG at 80 °C, a mixture containing 1 mmol phenyl boronic acid, 1 mmol aryl halide, 3 mmol potassium carbonate, and 0.005 g of the $\text{Fe}_3\text{O}_4@\text{xSiO}_2@\text{ySiO}_2@\text{BisPyP-Ni}$ (1.4 mol%) were heated until the end of the crude material consumption affirmed via thin layer chromatography (TLC). After the appropriate period, the resulting mixture was cooled to ambient temperature, and the catalyst was separated in the vicinity of the external magnetic field. Then, the organic layer was dried over sodium sulfate (2.5 g), and pure biphenyl derivatives were produced through solvent evaporation with excellent yields (Scheme 2).

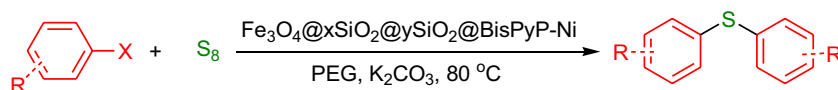
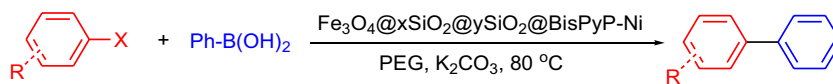
2.4 Typical Approach for the Production of Symmetric Diaryl Sulfides

In PEG at 80 °C, a mixture of $\text{Fe}_3\text{O}_4@\text{xSiO}_2@\text{ySiO}_2@\text{BisPyP-Ni}$ (0.005 g), 1 mmol aryl halide, 0.5 mmol sulfur, and 3 mmol potassium carbonate were heated until the end of the crude material consumption confirmed via TLC. After the appropriate time, the resulting mixture was cooled to ambient temperature, and the catalyst was separated in the vicinity of the external magnetic field. Subsequently, the filtrated solution with EtOAc was extracted. In the last step, the organic layer was dried with Na_2SO_4 , and the solvent was evaporated to give pure diaryl sulfides (Scheme 3).



Scheme 1 Preparation of $\text{Fe}_3\text{O}_4@\text{xSiO}_2@\text{ySiO}_2@\text{BisPyP-Ni}$

Scheme 2 $\text{Fe}_3\text{O}_4@\text{xSiO}_2@\text{ySiO}_2@\text{BisPyP-Ni}$ catalyzed the Suzuki–Miyaura reaction



Scheme 3 $\text{Fe}_3\text{O}_4@\text{xSiO}_2@\text{ySiO}_2@\text{BisPyP-Ni}$ catalyzed the production of di-aryl sulfides

3 Results and Discussion

In a continuous endeavor to develop novel synthetic processes, after successful fabrication of the catalyst, the synthesized nanocatalyst ($\text{Fe}_3\text{O}_4@x\text{SiO}_2@y\text{SiO}_2@\text{BisPyP-Ni}$) has been characterized using X-ray diffraction (XRD), Scanning electron microscopy (SEM), Transmission electron

microscopy (TEM), Energy-dispersive X-ray spectroscopy (EDX), Inductively Coupled Plasma (ICP), Vibrating sample magnetometer (VSM), Thermogravimetric analysis (TGA), Fourier-transform infrared spectroscopy (FT-IR), and adsorption/desorption porosimetry {Brunauer-Emmett-Teller (BET), Barrett-Joyner-Halenda (BJH), and adsorption/desorption isotherm} techniques.

3.1 XRD Analysis

Figure 1 shows the XRD patterns of $\text{Fe}_3\text{O}_4@x\text{SiO}_2@y\text{SiO}_2@\text{BisPyP-Ni}$, and $\text{Fe}_3\text{O}_4@\text{SiO}_2$ nanoparticles. As can be seen, these patterns show characteristic peaks related to Fe_3O_4 at $2\theta = 29.42^\circ$ (220), 33.74° (311), 41.47° (400), 55.82° (422), 59.08° (511), and 64.82° (440) [31, 32], and the broad peak appearing at $2\theta = 17\text{--}29^\circ$ with the equivalent Bragg angle at $2\theta \approx 23.83^\circ$ is related to the presence of silica layers around the nanoparticles [33]. Nickel particles correspond to the corresponding peaks at $2\theta = 48.31^\circ$ (111), 51.65° (200), and 72.47° (220) [33, 34]. These evidences indicate that nickel is well anchored on the nanocatalyst.

3.2 SEM and TEM Analyses

As can be seen from the SEM images of Fe_3O_4 and $\text{Fe}_3\text{O}_4@x\text{SiO}_2@y\text{SiO}_2@\text{BisPyP-Ni}$ samples (Fig. 2a and b, respectively), these materials are quasi-spherical in shape. The SEM image of $\text{Fe}_3\text{O}_4@x\text{SiO}_2@y\text{SiO}_2@\text{BisPyP-Ni}$ (Fig. 2b) shows that the composite is composed of homogeneous nanometre-sized particles (15.54–62.34 nm), and there are

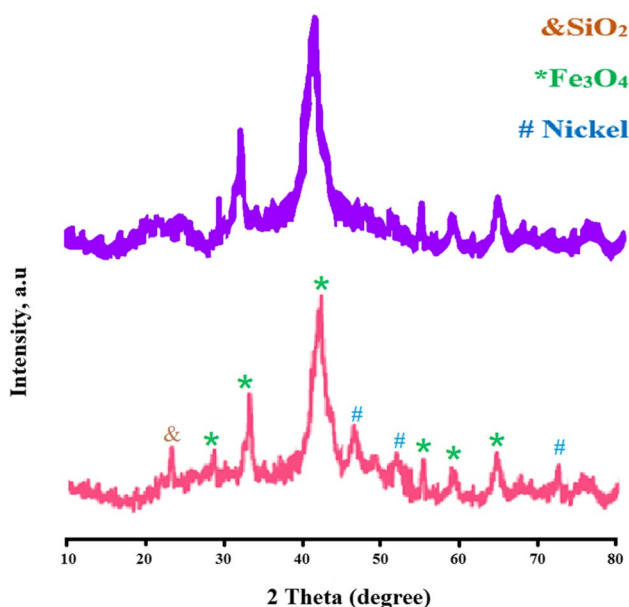


Fig. 1 The XRD pattern of $\text{Fe}_3\text{O}_4@x\text{SiO}_2@y\text{SiO}_2@\text{BisPyP-Ni}$ (a), and $\text{Fe}_3\text{O}_4@\text{SiO}_2$ (b)

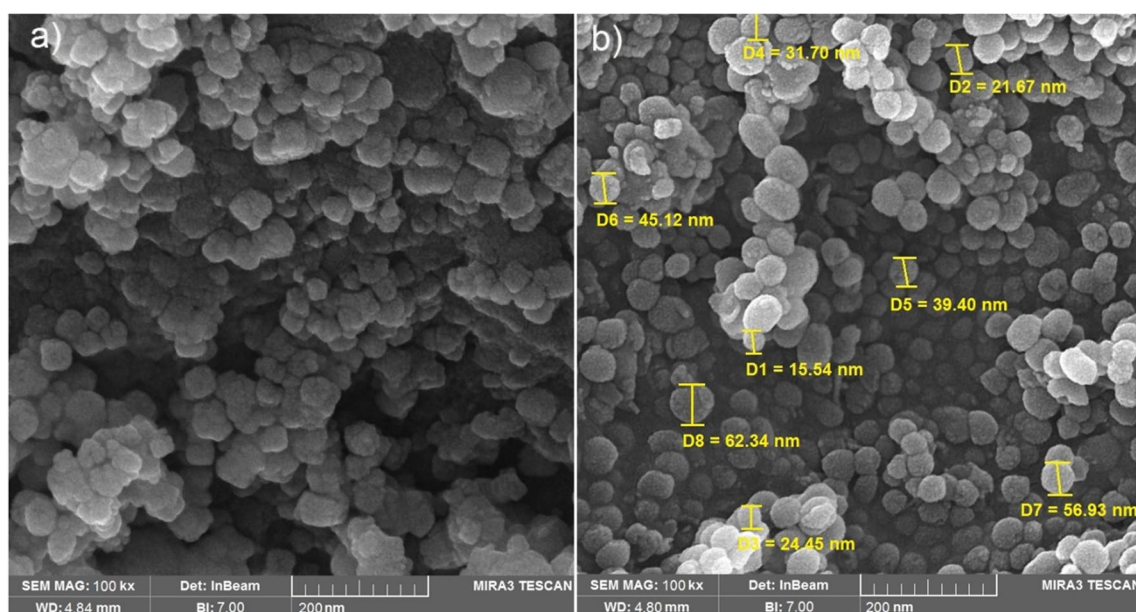


Fig. 2 SEM images of Fe_3O_4 (a) and $\text{Fe}_3\text{O}_4@x\text{SiO}_2@y\text{SiO}_2@\text{BisPyP-Ni}$ (b)

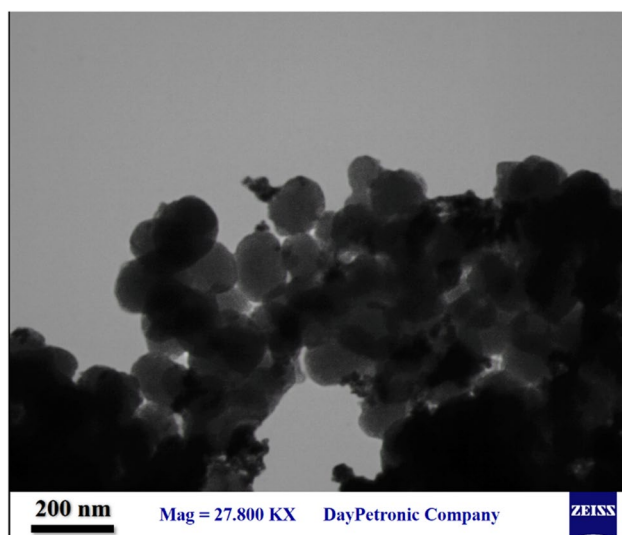


Fig. 3 SEM image of $\text{Fe}_3\text{O}_4@x\text{SiO}_2@y\text{SiO}_2@BisPyP-Ni$

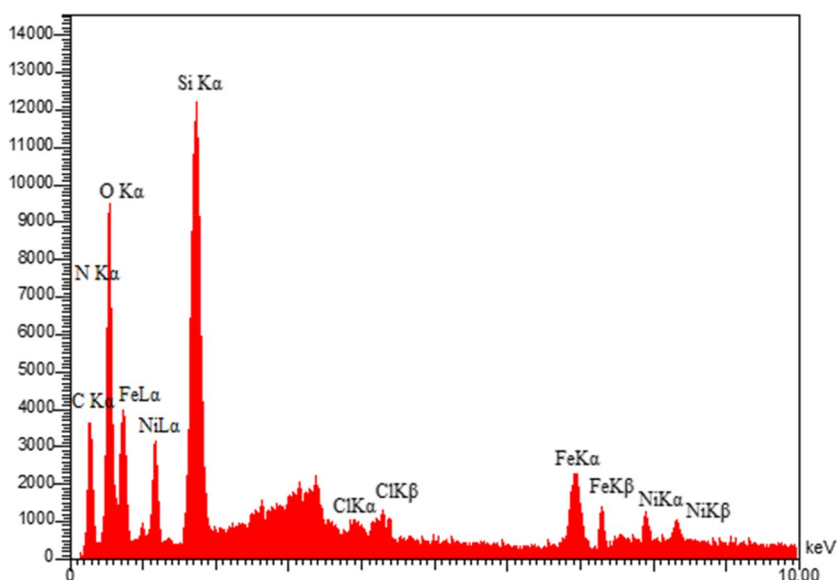
no visible changes in surface morphology when the Ni complex is put onto Fe_3O_4 .

The morphology of $\text{Fe}_3\text{O}_4@x\text{SiO}_2@y\text{SiO}_2@BisPyP-Ni$ was investigated using TEM method (Fig. 3). The image demonstrate that the catalyst particles are quasi-spherical shape, which amply supports the conclusions drawn from the SEM image.

3.3 EDS and ICP Analysis

The EDX analysis of $\text{Fe}_3\text{O}_4@x\text{SiO}_2@y\text{SiO}_2@BisPyP-Ni$ (Fig. 4) reveals that the Ni particles are equally dispersed over the Fe_3O_4 surface, which is compatible with the XRD pattern. In addition, the EDX spectrum of the catalyst

Fig. 4 EDX spectrum of $\text{Fe}_3\text{O}_4@x\text{SiO}_2@y\text{SiO}_2@BisPyP-Ni$



revealed the presence of N, C, O, Si, Fe, Cl and Ni species in the catalyst. The precise quantity of Ni placed on the mesoporous catalyst was also measured using ICP analysis, and it turned out to be $2.80 \times 10^{-3} \text{ mol g}^{-1}$.

3.4 VSM Analysis

The saturation magnetization of the Fe_3O_4 MNPs and the $\text{Fe}_3\text{O}_4@x\text{SiO}_2@y\text{SiO}_2@BisPyP-Ni$ were determined using vibrating sample magnetometry (Fig. 5), which shows that the Fe_3O_4 MNPs are ferromagnetic with a saturation magnetization of 72.19 emu g^{-1} , while the saturation magnetization of the nanocatalyst is 38.31 emu g^{-1} . The slight decrease observed in the saturation magnetization of $\text{Fe}_3\text{O}_4@x\text{SiO}_2@y\text{SiO}_2@BisPyP-Ni$ is due to the successful grafting of $x\text{SiO}_2@y\text{SiO}_2@BisPyP-Ni$ on the surface of Fe_3O_4 MNPs nanoparticles.

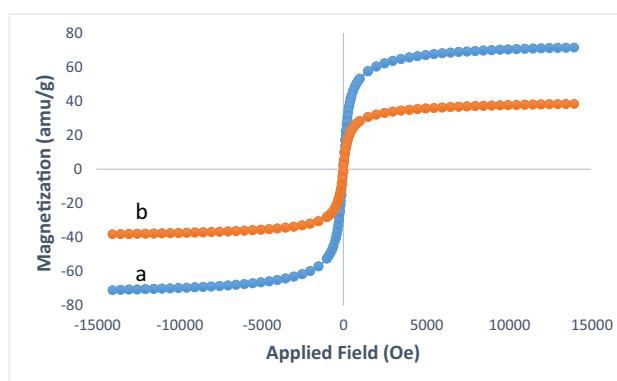


Fig. 5 Magnetization curves for $\text{Fe}_3\text{O}_4@x\text{SiO}_2@y\text{SiO}_2@BisPyP-Ni$ (a) and Fe_3O_4 (b)

3.5 TGA Analysis

TGA curve was also used to investigate the anchoring of BisPyP-Ni organometallic complex on Fe_3O_4 NMP. The TGA diagram of the $\text{Fe}_3\text{O}_4@x\text{SiO}_2@y\text{SiO}_2@z\text{BisPyP-Ni}$ is given in Fig. 6, which shows a three-stage mass reduction as the temperature increases. The first stage exhibits a minor mass loss (approximately 2%) at temperatures below 200 °C, which is attributed to the elimination of solvents adsorbed on the support. The second and third phases, between 200 and 460 °C and 460–700 °C, with (approximately 10% and 9%) weight loss, are attributable to organic layer breakdown and silanol group decomposition, respectively [30, 33].

3.6 FT-IR Analysis

FT-IR spectroscopy is a valuable tool for determining the molecular structure of organometallic complexes. Table 1; Fig. 7 summarize the FT-IR results of the $\text{Fe}_3\text{O}_4@x\text{SiO}_2$ (i), $\text{Fe}_3\text{O}_4@x\text{SiO}_2@y\text{SiO}_2@z\text{BisPyP}$ (ii), and $\text{Fe}_3\text{O}_4@x\text{SiO}_2@y\text{SiO}_2@z\text{BisPyP-Ni}$ (iii). These results support the formation of $\text{Fe}_3\text{O}_4@x\text{SiO}_2@y\text{SiO}_2@z\text{BisPyP-Ni}$, the immobilization of bilayer-SiO₂ on Fe_3O_4 , and the existence of the

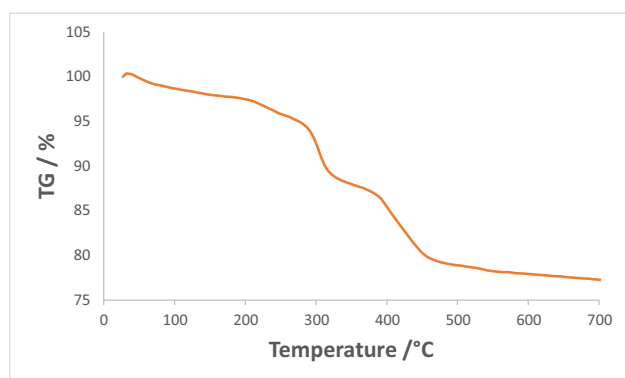


Fig. 6 TGA analysis of $\text{Fe}_3\text{O}_4@x\text{SiO}_2@y\text{SiO}_2@z\text{BisPyP-Ni}$

Table 1 The FT-IR data of $\text{Fe}_3\text{O}_4@x\text{SiO}_2$ (i), $\text{Fe}_3\text{O}_4@x\text{SiO}_2@y\text{SiO}_2@z\text{BisPyP}$ (ii), and $\text{Fe}_3\text{O}_4@x\text{SiO}_2@y\text{SiO}_2@z\text{BisPyP-Ni}$ (iii)

Absorption (cm^{-1})	Related bond
610 (i), 620 (ii), 618 (iii)	stretching of Fe–O
785 (i), ~795 (ii), 779 (iii)	symmetric stretching of Si–O–Si
974 (i), ~990 (ii), ~990 (iii)	stretching of Si–O–Fe
1080 (i), 1119 (ii), 1111 (iii)	asymmetric stretching of Si–O–Si
1388 (ii), 1387 (iii)	stretching of C–N
1456 (ii), 1456 (iii)	bending of CH_2
1488 (ii), 1488 (iii)	stretching of C=C
1668 (ii), 1660 (iii)	stretching of C=N
1643 (i), 1630 (ii), ~1630 (iii)	OH bending on the surface of the SiO_2 and Fe_3O_4
2934 (ii), 2949 (iii)	C–H symmetric stretching
3422 (i), 3419 (ii), 3423 (iii)	OH stretching on the surface of the SiO_2 and Fe_3O_4

predicted bonds. The anchoring of Ni to $\text{Fe}_3\text{O}_4@x\text{SiO}_2@y\text{SiO}_2@z\text{BisPyP}$ was confirmed with a shift of C=N vibration stretching in $\text{Fe}_3\text{O}_4@x\text{SiO}_2@y\text{SiO}_2@z\text{BisPyP-Ni}$ (1660 cm^{-1}), compared to $\text{BisPyP@bilayer-SiO}_2@z\text{NMP}$ (1668 cm^{-1}), to a lower frequency which is the reason for this shift is the coordination of Ni to supported BisPyP onto functionalized $\text{Fe}_3\text{O}_4@x\text{SiO}_2@y\text{SiO}_2$ [33, 35, 36].

3.7 Nitrogen adsorption-desorption Analysis

The porosity of $\text{Fe}_3\text{O}_4@x\text{SiO}_2@y\text{SiO}_2@z\text{BisPyP-Ni}$ nanocomposite and its parents were examined via the nitrogen adsorption-desorption method (Figs. 8, 9, and 10). The information obtained from this technique was tabulated in Table 2. According to the findings in the table, $\text{Fe}_3\text{O}_4@x\text{SiO}_2@y\text{SiO}_2@z\text{BisPyP-Ni}$ has a lower specific surface area than $\text{Fe}_3\text{O}_4@x\text{SiO}_2@y\text{SiO}_2@z\text{BisPyP}$, $\text{Fe}_3\text{O}_4@x\text{SiO}_2$, and Fe_3O_4 . This is because Ni complex and organic groups have anchored on the mesoporous channels of the substrate nanoparticles. The good bonding of organic skeleton and metal complex on the Fe_3O_4 is confirmed based on these findings.

3.8 Catalytic Studies

After the production and identification of $\text{Fe}_3\text{O}_4@x\text{SiO}_2@y\text{SiO}_2@z\text{BisPyP-Ni}$ catalyst, its catalytic activity in forming C–C bond (through Suzuki reaction) and C–S bond was studied.

At first, to find the best circumstances for C–C coupling, the reaction of 1 mmol phenylboronic acid (PhB(OH)_2) with 1 mmol 4-methyl iodobenzene was elected as a model. Then, the result of various factors on its efficiency and time was investigated (Table 3), such as the nature of the solvent {by examining the performance of solvents e.g., 1,4-dioxane, water, ethanol, dimethylformamide (DMSO), dimethyl sulfoxide (DMF) and PEG-400} (Table 3, entries 1–6), type of base {including 4-dimethylaminopyridine (DMAP), Et_3N , KOH, NaOH, K_2CO_3 and KHCO_3 } (Table 3, entries 6–11),

Fig. 7 The FT-IR spectra of $\text{Fe}_3\text{O}_4@\text{SiO}_2$ (i), $\text{Fe}_3\text{O}_4@x\text{SiO}_2@y\text{SiO}_2@\text{BisPyP}$ (ii), and $\text{Fe}_3\text{O}_4@x\text{SiO}_2@y\text{SiO}_2@\text{BisPyP-Ni}$ (iii)

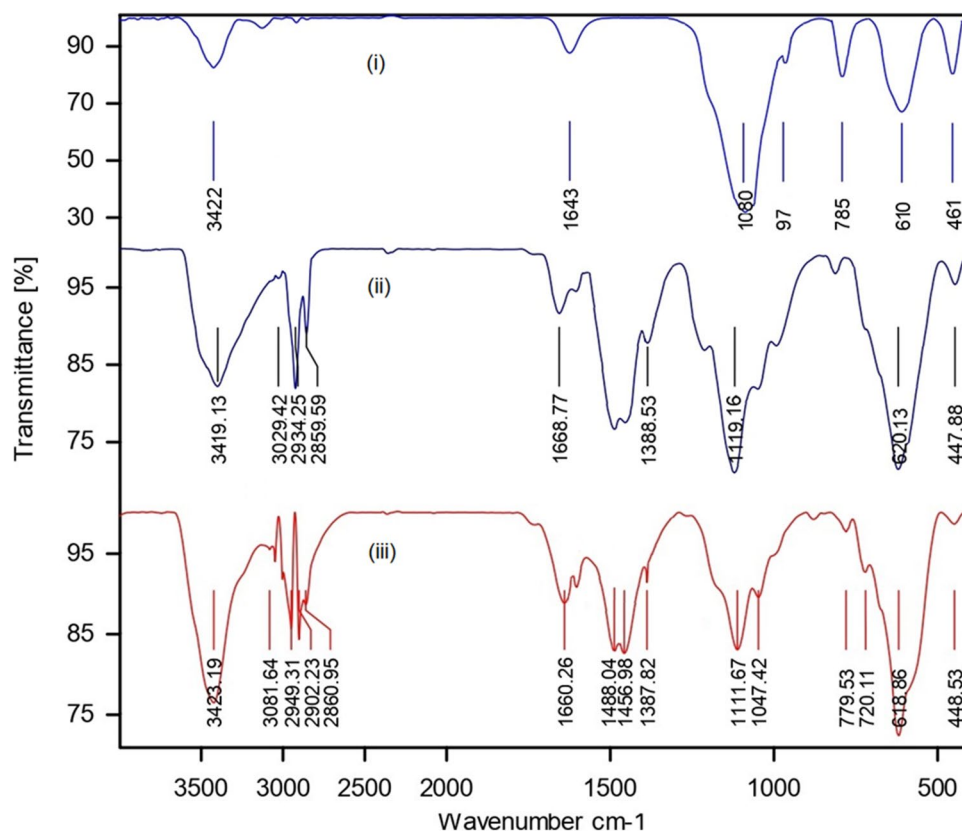
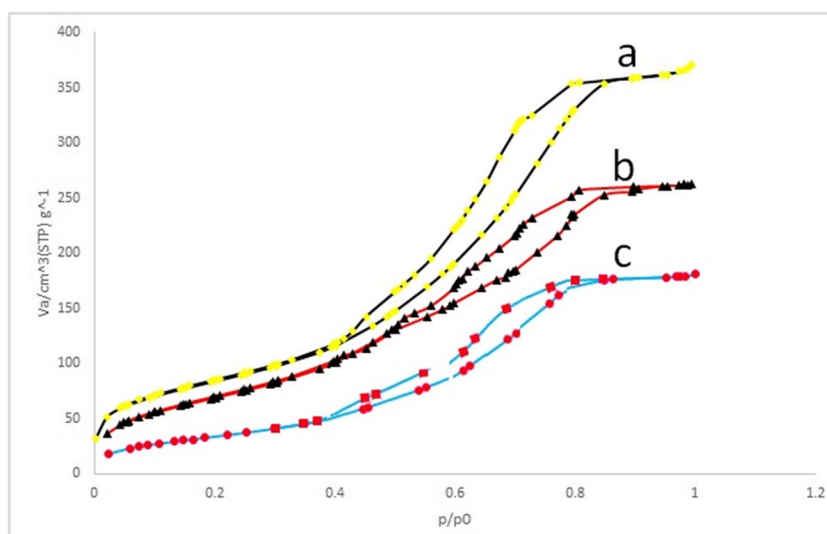


Fig. 8 Nitrogen adsorption-desorption isotherms of $\text{Fe}_3\text{O}_4@x\text{SiO}_2$ (a), $\text{Fe}_3\text{O}_4@x\text{SiO}_2@y\text{SiO}_2@\text{BisPyP}$ (b), and $\text{Fe}_3\text{O}_4@x\text{SiO}_2@y\text{SiO}_2@\text{BisPyP-Ni}$ (c)



the amount of catalyst {using amounts of 4, 5 and 6 mg of catalyst} (Table 3, entries 6, 16 and 17), and temperature {in the range of 25–100 °C} (Table 3, entries 6, 13, 14 and 15). The screening of the mentioned solvents showed that PEG-400 is the best solvent for the progress of the model reaction (Table 3, entry 6). This is probably due to its influential role in reducing Ni(II) to Ni(0), which has been reported in the literature [38, 39]. Among the considered

bases, it is found that K_2CO_3 acts as an excellent base for this reaction (Table 3, entry 6). It is noteworthy that the higher performance of our catalyst with bases such as K_2CO_3 and KHCO_3 , since according to the studies of Knecht and co-workers [40], although for monobasics such as NaOH or KOH, the amount of reactive and free hydroxide is higher compared to dibasic systems such as K_2CO_3 and KHCO_3 , but this leads to their potent combination with Nickel metal

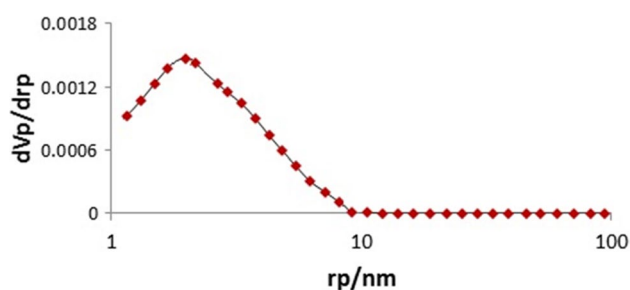


Fig. 9 The pore size distribution (BJH model) of $\text{Fe}_3\text{O}_4@x\text{SiO}_2@y\text{SiO}_2@BisPyP-Ni$

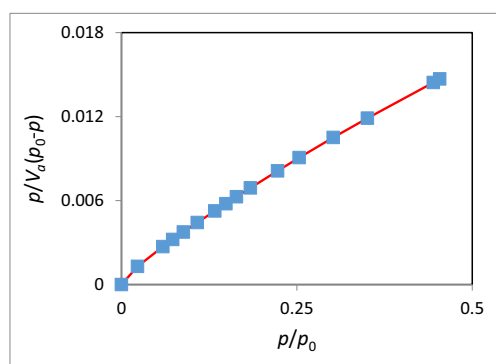


Fig. 10 The BET curve of $\text{Fe}_3\text{O}_4@x\text{SiO}_2@y\text{SiO}_2@BisPyP-Ni$

species, and finally reducing the yield of biphenyl. Also, organic bases such as DMAP and Et_3N are not strong enough for this cross-coupling reaction. Accordingly, a moderate base capacity is essential for the coupling reaction in the presence of a catalytic amount of $\text{Fe}_3\text{O}_4@x\text{SiO}_2@y\text{SiO}_2@BisPyP-Ni$. Hence, when K_2CO_3 and KHCO_3 are considered, a different trend in reactivity is seen, with higher product yields compared to potassium hydroxide, sodium hydroxide, or organic bases.

Also, the reaction failed in the absence of a suitable solvent (Table 3, entry 1), without base (Table 3, entry 12), at ambient temperature (Table 3, entry 13), and under catalyst-free conditions (Table 3, entry 18), so the optimal use of these four items is necessary to produce the biphenyl derivative. Finally, the findings from the Table 3 revealed that the optimum conditions in the model reaction are obtained

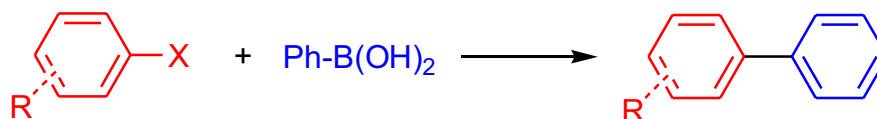
using K_2CO_3 as base (3 mmol) and 5 mg of $\text{Fe}_3\text{O}_4@x\text{SiO}_2@y\text{SiO}_2@BisPyP-Ni$ in PEG-400 solvent (2 mL) at 80 °C (Table 3, entry 6).

In an interesting study, after the optimal circumstances, the progress of the model reaction was checked with the catalyst parents, namely: Fe_3O_4 (Table 4, entry 1), $\text{Fe}_3\text{O}_4@x\text{SiO}_2@y\text{SiO}_2$ (Table 4, entry 2), $\text{Fe}_3\text{O}_4@x\text{SiO}_2@y\text{SiO}_2@BisPyP$ (Table 4, entry 3), and also $\text{Fe}_3\text{O}_4@x\text{SiO}_2@BisPyP-Ni$ {In the construction of this catalyst, unlike our catalyst, a silicon shell has been used around the magnetic core} (Table 4, entry 4). After that, the amount of nickel loaded in $\text{Fe}_3\text{O}_4@x\text{SiO}_2@y\text{SiO}_2@BisPyP-Ni$ and $\text{Fe}_3\text{O}_4@x\text{SiO}_2@BisPyP-Ni$ calculated through the ICP method, which was equal to 2.80×10^{-3} and $1.50 \times 10^{-3} \text{ mol g}^{-1}$, respectively. The conclusions reached from the ICP method and Table 4 prove that the idea of utilizing bi-layers of silica around magnetic iron oxide nanoparticles and anchoring nickel metal on the $\text{Fe}_3\text{O}_4@x\text{SiO}_2@y\text{SiO}_2@BisPyP$ was helpful in promoting the coupling reaction, because the C-C coupling reaction with the raw materials of catalyst generation led to zero yield (Table 4, entries 1–3), and only when the final catalyst is formed with all parent compounds, a powerful synergetic effect of the catalyst became apparent. Covering magnetic nanoparticles with two silica shells, apart from keeping the magnetic nanoparticles from aggregation, causes more organic ligands (organic groups) and thus more Ni to join the mesoporous cavities, and the reaction is completed with a lower mol% of the catalyst.

Afterwards, determining the best circumstances to perform the model reaction, the range of catalytic activity of $\text{Fe}_3\text{O}_4@x\text{SiO}_2@y\text{SiO}_2@BisPyP-Ni$ was evaluated through the reaction of PhB(OH)_2 with different aryl halides. The findings are tabulated in Table 5. It was ascertained that $\text{Fe}_3\text{O}_4@x\text{SiO}_2@y\text{SiO}_2@BisPyP-Ni$ is a very effective catalyst for obtaining the corresponding biphenyl derivative. All the aryl halides used, regardless of the electron-donating or -withdrawing nature of their attached substituents, provided the corresponding derivatives in excellent yields and times. However, iodide- and bromide-substituted aryl halides gave better results compared to chloride-substituted aryl halides, because iodide and bromide are stronger leaving groups than chloride (Table 5, Inputs 1a and 7a vs. 18a). Also, the presence of ortho-substituents led to slower product formation compared to para-substituents, which was attributed to

Table 2 Texture properties of the prepared samples

Sample	SBET (m^2/g)	Pore diam by BJH method (nm)	Pore vol (cm^3/g)	Ref.
Fe_3O_4	480.0	1.254	0.803	[37]
$\text{Fe}_3\text{O}_4@x\text{SiO}_2$	462.8	1.701	0.732	-
$\text{Fe}_3\text{O}_4@x\text{SiO}_2@y\text{SiO}_2@BisPyP$	398.7	1.989	0.701	-
$\text{Fe}_3\text{O}_4@x\text{SiO}_2@y\text{SiO}_2@BisPyP-Ni$	347.9	2.222	0.618	-

Table 3 C–C coupling of 4-methyliodobenzene with PhB(OH)₂ using Fe₃O₄@xSiO₂@ySiO₂@BisPyP-Ni under different conditions

Entry	Solvent	Base (mmol)	Temperature (°C)	Catalyst (mg)	Time (min)	Yield (%) ^a
1	1,4-Dioxane	K ₂ CO ₃	80	5	15	—
2	EtOH	K ₂ CO ₃	Reflux	5	15	24
3	H ₂ O	K ₂ CO ₃	80	5	15	21
4	DMSO	K ₂ CO ₃	80	5	15	66
5	DMF	K ₂ CO ₃	80	5	15	70
6	PEG	K ₂ CO ₃	80	5	15	98
7	PEG	Et ₃ N	80	5	15	22
8	PEG	DMAP	80	5	15	25
9	PEG	KOH	80	5	15	61
10	PEG	NaOH	80	5	15	44
11	PEG	KHCO ₃	80	5	15	82
12	PEG	—	80	5	360	—
13	PEG	K ₂ CO ₃	25	5	240	—
14	PEG	K ₂ CO ₃	60	5	90	54
15	PEG	K ₂ CO ₃	100	5	5	98
16	PEG	K ₂ CO ₃	80	4	60	74
17	PEG	K ₂ CO ₃	80	6	5	98
18	PEG	K ₂ CO ₃	80	—	1440	—

Reaction conditions: PhB(OH)₂ (1 mmol), 4-methyliodobenzene (1 mmol), solvent (2 mL), base (3 mmol)

^aIsolated yield

Table 4 Checking impact of Fe₃O₄, Fe₃O₄@xSiO₂@ySiO₂, Fe₃O₄@xSiO₂@ySiO₂@BisPyP and Fe₃O₄@xSiO₂@BisPyP-Ni in coupling of 4-methyliodobenzene with PhB(OH)₂

Entry	Catalyst	Yield (%) ^a
1	Fe ₃ O ₄	— ^b
2	Fe ₃ O ₄ @xSiO ₂ @ySiO ₂	— ^b
3	Fe ₃ O ₄ @xSiO ₂ @ySiO ₂ @BisPyP	— ^b
4	Fe ₃ O ₄ @xSiO ₂ @BisPyP-Ni	66

^aIsolated yield under optimized conditions

^bNo reaction

increased steric hindrance (Table 5, entry 2a vs. 3a and entry 4a vs. 5a).

In the second part of our study, after successfully using Fe₃O₄@xSiO₂@ySiO₂@BisPyP-Ni as a catalyst in the generation of C–C bond (via Suzuki reaction), we decided to test its catalytic activity to obtain symmetric diaryl sulfides. In this regard, the effect of various factors, including the nature of the solvent, temperature and the type of base, and the amount of nano-catalyst on the model reaction (i.e., 2 mmol of 4-methyliodobenzene with 1 mmol of S₈) was monitored.

The findings are tabulated in Table 6. As the table shows, the best conditions for performing the reaction were obtained when the reaction was carried out using K₂CO₃ base (4 mmol) and 5 mg of Fe₃O₄@xSiO₂@ySiO₂@BisPyP-Ni at 80 °C in 2 mL of PEG-400 (Table 6, entry 6).

Next, diverse aryl halides (comprising aryl bromides, aryl iodides, and aryl chloride) were reacted with S₈ under optimal conditions to determine the catalytic capability and scope of Fe₃O₄@xSiO₂@ySiO₂@BisPyP-Ni with this method (Table 7, entries 1b–10b). As Table 7 shows, various types of substituted aryl halides with electron-accepting and electron-donating groups were successfully coupled with S₈, and provided the corresponding products in 20–140 min with yields of 79–98%. As expected, aryl iodides gave the best yields at shorter reaction times compared to aryl bromides and aryl chlorides in this reaction, because iodide is a stronger leaving group than bromide and chloride (Table 7, Input 1b vs. 2b and 3b). Meanwhile, in this reaction (like the Suzuki reaction), the role of reducing the steric hindrance around the halogen-carrying carbon was evident in accelerating the formation of the product (Table 7, Input 4b vs. 6b).

The following mechanism can be provided for the investigated catalytic system based on research done in the area of

Table 5 C-C coupling from Suzuki reaction via $\text{Fe}_3\text{O}_4@\text{xSiO}_2@\text{ySiO}_2@\text{BisPyP-Ni}$

Entry	R	X	Time (min)	Yield (%) ^a	M.p. (°C)		TOF(min ⁻¹) ^b
					Found	Reported	
1a	H	I	15	98	67–69	68–70 [41]	4.666
2a	4-OCH ₃	I	20	96	88–90	88–90 [41]	3.428
3a	2-OCH ₃	I	25	94	Colorless oil	Colorless oil [42]	2.685
4a	4-CH ₃	I	15	98	44–46	44–46 [41]	4.666
5a	2-CH ₃	I	20	95	Light yellow liquid	Light yellow liquid [42]	3.3928
6a	2-CO ₂ H	I	17	98	106–108	107–109 [43]	4.117
7a	H	Br	17	97	67–69	68–70 [41]	4.075
8a	4-CH ₃	Br	17	98	45–47	44–46 [41]	4.116
9a	4-OH	Br	20	97	162–164	163–164 [44]	3.464
10a	4-CHO	Br	20	96	54–56	54–56 [45]	3.428
11a	4-CN	Br	25	98	85–87	85–86 [44]	2.799
12a	4-CO ₂ H	Br	26	93	225–227	224–228 [46]	2.554
13a	4-NO ₂	Br	18	98	110–112	112–114 [41]	3.888
14a	4-NH ₂	Br	20	97	50–52	50–53 [45]	3.464
15a	4-SH	Br	25	94	110–112	110–111 [47]	2.685
16a	3-CHO	Br	25	95	52–54	53–54 [48]	2.714
17a	4-Cl	Br	25	94	70–72	71–73 [49]	2.685
18a	H	Cl	30	92	161–163	163–164 [44]	2.190

Reaction conditions: PhB(OH)_2 (1 mmol), base (3 mmol), aryl halide (1 mmol), PEG-400 (2 mL), $\text{Fe}_3\text{O}_4@\text{xSiO}_2@\text{ySiO}_2@\text{BisPyP-Ni}$ (5 mg, 1.4 mol%)

^aIsolated yield

^bTurnover frequency (TOF) is defined as mole of produced product per mole of catalyst per time⁻¹

the production aryl halides from the reaction of S_8 with aryl halides in the proximity of nickel catalyst [52] (Scheme 4). S_8 (the sulfur source) combines with potassium hydroxide in the first stage to create potassium disulfide. Then, the reaction between the potassium disulfide and the $\text{Fe}_3\text{O}_4@\text{xSiO}_2@\text{ySiO}_2@\text{BisPyP-Ni}$, leads to nickel disulfide. In the subsequent step, an oxidative-addition reaction with aryl halide causes nickel disulfide to change into intermediate **I**. Then, a reductive-elimination reaction results in the production of intermediate **II**. The subsequent stage is an oxidative-addition process in which intermediate **II** and aryl halide produce intermediate **III**. The $\text{Fe}_3\text{O}_4@\text{xSiO}_2@\text{ySiO}_2@\text{BisPyP-Ni}$ returns to the catalytic cycle in the last stage, where it participates in a reductive-elimination process to form the diaryl sulfide product.

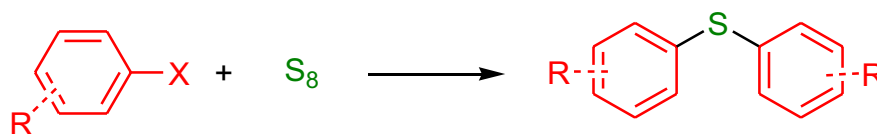
3.9 Reusability Investigation of the Catalyst

For industrial applications, reusable catalysts are required. As a consequence, the recyclability of $\text{Fe}_3\text{O}_4@\text{xSiO}_2@$

$\text{ySiO}_2@\text{BisPyP-Ni}$ was investigated in the carbon-carbon coupling reaction leading to the production of 4-methoxy-1,1'-biphenyl (**2a**). In this regard, after the completion of the reaction, by using an external magnet to hold the spent catalyst on the bottom of the reaction vessel, the reaction solution was easily decanted as shown in Scheme 5. Then, the catalyst was cleaned with ethyl acetate, and dried for use in the next run. As illustrated in Fig. 11, the catalyst can be reutilized up to eight times without losing substantial activity.

3.10 Investigation of Catalyst Leaching

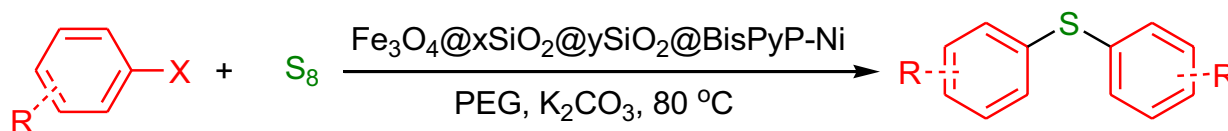
Hot filtration experiments were carried out in the coupling of 4-methyl iodobenzene with PhB(OH)_2 to check the leaching of $\text{Fe}_3\text{O}_4@\text{xSiO}_2@\text{ySiO}_2@\text{BisPyP-Ni}$ (having bilayer SiO_2), $\text{Fe}_3\text{O}_4@\text{xSiO}_2@\text{BisPyP-Ni}$ (having monolayer SiO_2), under optimal conditions. In these two studies, 65% and 36% of the product were produced after 7.5 min with bilayer and monolayer silica catalysts,

Table 6 C–S coupling of 4-methyliodobenzene with S_8 via $Fe_3O_4@xSiO_2@ySiO_2@BisPyP-Ni$ under different conditions

Entry	Solvent	Base (mmol)	Temperature (°C)	Catalyst (mg)	Time (min)	Yield (%) ^a
1	1,4-Dioxane	K ₂ CO ₃	80	5	30	84
2	EtOH	K ₂ CO ₃	Reflux	5	30	90
3	H ₂ O	K ₂ CO ₃	80	5	30	90
4	DMSO	K ₂ CO ₃	80	5	30	98
5	DMF	K ₂ CO ₃	80	5	30	95
6	PEG	K ₂ CO ₃	80	5	30	98
7	PEG	Et ₃ N	80	5	30	31
8	PEG	DMAP	80	5	30	40
9	PEG	KOH	80	5	30	70
10	PEG	NaOH	80	5	30	66
11	PEG	KHCO ₃	80	5	30	86
12	PEG	K ₂ CO ₃	25	5	240	—
13	PEG	K ₂ CO ₃	60	5	120	62
14	PEG	K ₂ CO ₃	110	5	30	98
15	PEG	K ₂ CO ₃	80	4	90	78
16	PEG	K ₂ CO ₃	80	6	30	98
17	PEG	K ₂ CO ₃	80	—	2880	—

Reaction conditions: 4-methyliodobenzene (2 mmol), S_8 (1 mmol), solvent (2 mL), base (4 mmol)

^aIsolated yield

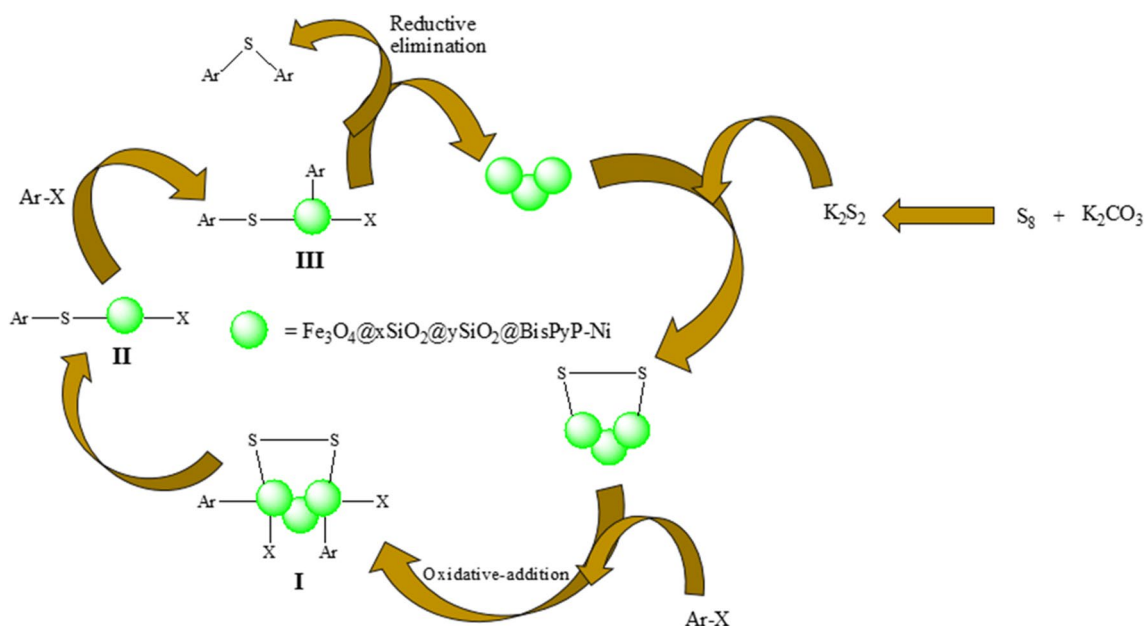
Table 7 C–S coupling of aryl halides with S_8 catalyzed using $Fe_3O_4@xSiO_2@ySiO_2@BisPyP-Ni$ 

Entry	R	X	Time (min)	Yield (%) ^a	M.p. (°C)		TOF(min ⁻¹) ^b
					Found	Reported	
1b	H	I	20	98	Oil	Oil [50]	3.499
2b	H	Br	50	91	Oil	Oil [50]	1.300
3b	H	Cl	140	79	Oil	Oil [50]	0.403
4b	4-OCH ₃	I	35	97	Oil	Oil [50]	1.979
5b	4-OCH ₃	Br	60	96	Oil	Oil [50]	1.142
6b	2-OCH ₃	I	70	95	Oil	Oil [50]	0.969
7b	4-CH ₃	I	80	97	Oil	Oil [50]	0.866
8b	4-CH ₃	Br	90	95	Oil	Oil [50]	0.753
9b	4-NO ₂	Br	20	90	156–158	157–159 [51]	3.214
10b	4-CF ₃	I	55	93	Oil	Oil [50]	1.207

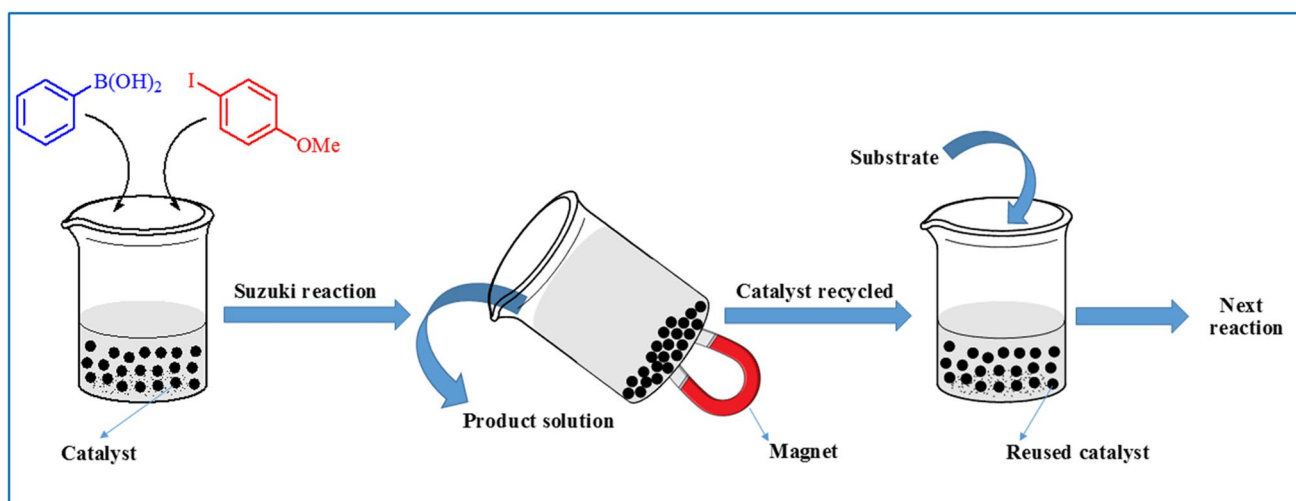
Reaction conditions: aryl halide (2 mmol), S_8 (1 mmol), base (4 mmol), $Fe_3O_4@xSiO_2@ySiO_2@BisPyP-Ni$ (5 mg, 1.4 mol%), PEG-400 (2 mL)

^aIsolated yield

^bTurnover frequency (TOF) is defined as mole of produced product per mole of catalyst per time⁻¹



Scheme 4 The proposed mechanism for the synthesis of diaryl sulfides



Scheme 5 Separation of spent catalyst from the reaction solution via an external magnet

respectively. The same reactions were performed again, and at the half time of the reactions (after 7.5 min), the $\text{Fe}_3\text{O}_4@x\text{SiO}_2@y\text{SiO}_2@BisPyP-Ni$, and $\text{Fe}_3\text{O}_4@x\text{SiO}_2@y\text{SiO}_2@BisPyP$ were withdrawn, and the filtrated mixtures were allowed to run for an additional 7.5 min. At this point, 67% and 39% of the product had been collected with bilayer and monolayer silica catalysts, respectively. These observations prove the absence of nickel leaching and the influential role of using two layers of silica in the performance of our catalyst.

3.11 Comparison

To investigate the catalytic activity of fabricated $\text{Fe}_3\text{O}_4@x\text{SiO}_2@y\text{SiO}_2@BisPyP-Ni$, we compared its efficiency with the catalysts mentioned in past papers. Therefore, we checked the model reactions for the production of 1,1'-biphenyl (i) and diphenyl sulfide (ii) by reviewing parameters, e.g. reaction conditions, yield, and reaction time. As can be clearly seen in Table 8, our catalyst showcased excellent reaction times and yields.

Fig. 11 The recycling experiment of $\text{Fe}_3\text{O}_4@\text{xSiO}_2@\text{ySiO}_2@\text{BisPyP-Ni}$ in the synthesis of biphenyl

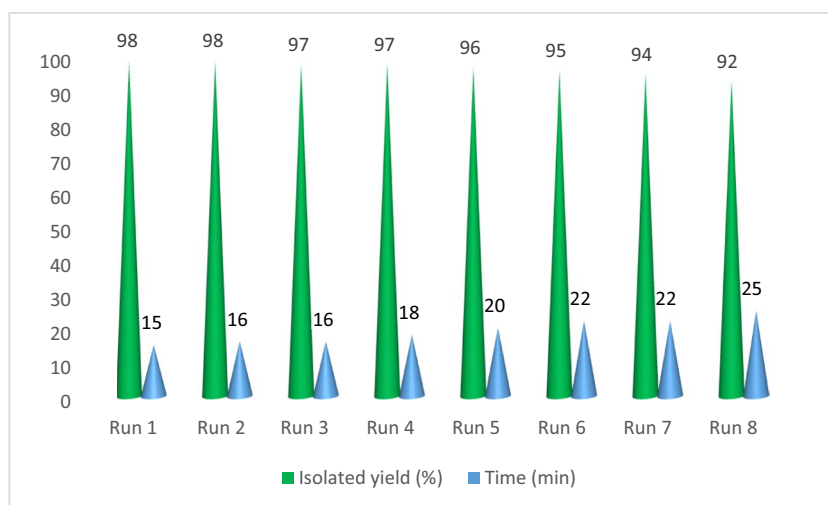


Table 8 Comparing catalytic activity of $\text{Fe}_3\text{O}_4@\text{xSiO}_2@\text{ySiO}_2@\text{BisPyP-Ni}$ with other catalysts for the synthesis of 1,1'-biphenyls (i) and diphenyl sulfides (ii)

Catalyst	Conditions	Type of reaction	Time (min)	Yield (%)	Ref.
$\text{Fe}_3\text{O}_4@\text{xSiO}_2@\text{ySiO}_2@\text{BisPyP-Ni}$	K_2CO_3 , PEG-400, 80 °C	i	15	98	This work
$\text{Fe}_3\text{O}_4@\text{xSiO}_2@\text{ySiO}_2@\text{BisPyP-Ni}$	K_2CO_3 , PEG-400, 80 °C	ii	20	98	This work
$\text{Fe}_3\text{O}_4@\text{SiO}_2\text{-T-Se/Pd (II)}$	K_2CO_3 , EtOH: H_2O , 60 °C	i	30	95	[53]
PdNP-PNF	DMSO, 130 °C, KOH	ii	300	92	[54]
$\text{Fe}_3\text{O}_4@\text{MCM-41}@Pd\text{-SPATB}$	K_2CO_3 , PEG, 80 °C	i	25	94	[31]
CuI, DBU	Toluene, 100 °C	ii	2880	85	[55]
Pd/chamomile@ Fe_3O_4	K_2CO_3 , EtOH: H_2O , 60 °C	i	60	96	[56]
CuI	NaOH, PEG200, 110 °C	ii	1080	84	[57]
GO/ Fe_3O_4 /PAMPS/Pd	PEG-400, 80 °C	i	120	100	[58]
CuI	NaOt-Bu, PEG200, 60–80 °C	ii	900	92	[59]
Pd-AcAc-Am- $\text{Fe}_3\text{O}_4@\text{SiO}_2$	K_2CO_3 , DMF: H_2O , 80 °C	i	60	96	[52]
Ni(II)-modified-SBA-15	DMSO, 120 °C, KOH	ii	84	96	[60]
CA/Pd(0)	K_2CO_3 , H_2O , Reflux	i	120	94	[61]
Ni-guanidine@MCM-41NPs	DMSO, 110 °C, KOH	ii	180	94	[50]
Pd/Au NPs	K_2CO_3 , EtOH/ H_2O , N_2 , 80 °C	i	1440	88	[62]
LDH-Pd(0)	K_2CO_3 , H_2O /Dioxan, Reflux	i	600	96	[63]

4 Conclusions

In conclusion, we portrayed an unsophisticated approach to anchor BisPyP-Ni complex onto the $\text{Fe}_3\text{O}_4@\text{xSiO}_2@\text{ySiO}_2$ substrate through covalent cross-linking. The composition and skeleton of the fabricated $\text{Fe}_3\text{O}_4@\text{xSiO}_2@\text{ySiO}_2@\text{BisPyP-Ni}$ were fully identified via XRD, SEM, EDS, ICP, VSM, TGA, FT-IR and nitrogen adsorption desorption techniques. In addition, the catalytic capability of this nanocatalyst was studied in C-C and C-S coupling using reaction of (i) aryl halides with S_8 , and (ii) aryl halides with PhB(OH)_2 in PEG-400 under environment-friendly

conditions, severally. Consequently, high porosity and surface area, the utilize of chemically and inexpensive stabile reagents, appropriate duplicability of the nano-catalyst up to 8 runs, operational simplicity, excellent reaction times and, ease of separation with an external magnetic field, makes the $\text{Fe}_3\text{O}_4@\text{xSiO}_2@\text{ySiO}_2@\text{BisPyP-Ni}$ a good candidate for potential uses in future research.

Supplementary Information The online version contains supplementary material available at <https://doi.org/10.1007/s12633-024-02959-0>.

Acknowledgements The authors are grateful to acknowledge the Takin Shimi Sepanta Industries Co, Ilam, Iran.

Author Contributions Ebraheem Abdu Musad Saleh: produced some C-C coupling products (1a-9a), and helped to edit the article. Asmaa F. Kassem: produced some C-C coupling products (10a-18a). Farag M. A. Altalbawy: produced some C-S coupling products (1b-5b). Sarah Jawad Shoja: produced some C-S coupling products (6b-10b). Bokov Dmitry Olegovich: optimized C-C coupling reaction. Ahmed Elawady: optimized C-S coupling reaction. Ameer H. Al-Rubaye: determined the structure of the nano-catalyst through EDS, TEM and SEM techniques. Abdunaser Saud: determined the structure of the nano-catalyst by ICP, BET and VSM techniques. Zuhair I. Al-Mashhadani: determined the structure of the nano-catalyst via TGA and XRD techniques. Maryam Sadat Ghorayshi Nejad: produced the nano-catalyst, and wrote the article.

Funding The authors expressly announce that no grants, funds, or other support were received during the preparing this paper.

Data Availability No datasets were generated or analysed during the current study.

Declarations

Ethics Approval and Consent to Participate The author's declare that the paper is not be submitted simultaneously to another journal. The submitted work is original and has not been published elsewhere in any form or language, and the authors have no conflict of interest regarding this manuscript. The authors agree to participate in submitting our manuscript to this journal, and agree to the publication of our research data in this journal.

Consent for Publication We have confirmed.

Competing Interests The authors declare no competing interests.

References


- Gebre SH (2023) *Appl Nanosci* 13:15
- Xie W, Li J (2023) *Renew Sustain Energy Rev* 171:113017
- Kumar P, Tomar V, Kumar D, Joshi RK, Nemiwal M (2022) *Tetrahedron* 106:132641
- Rossi LM, Costa NJ, Silva FP, Wojcieszak R (2014) *Green Chem* 16:2906
- Hafizi H, Rahman ML, Sarjadi MS, Akhter MS, Collins MN, O'Reilly EJ, Walker GM, Sarkar SM (2022) *Arab J Chem* 15:103914
- Ngcobo M, Ojwach SO (2021) *Mol Catal* 508:111583
- Niakan M, Karimi S, Masteri-Farahani M, Shekaari H (2021) *Colloids Surf a* 620:126603
- Zhao Q, Liang H, Huang S, Han X, Wang H, Wang J, Wang Y, Ma X (2021) *Catal Today* 368:133
- Ganjali F, Kashtiaray A, Zarei-Shokat S, Taheri-Ledari R, Maleki A (2022) *Nanoscale Adv* 4:1263
- Hafizi H, Walker G, Collins M (2022) *Renew Energy* 1:459
- Li Z, Dong J, Zhang Y, Zhuang T, Wang H, Du X, Cui X, Wang Z (2022) *Compos Sci Technol* 8:109198
- Binandeh M, Nasser MA, Allahresani A (2022) *Catalysts* 12:976
- Nejad MS, Seyedi N, Sheibani H, Behzadi S (2019) *Mol Divers* 23:527
- 18, Liu Z, Yuan D, Su Y (2023) *Catal Lett* 153:698
- Lou J, Wang Q, Wu P, Wang H, Zhou YG, Yu Z (2020) *Chem Soc Rev* 49:4307
- Kashin AS, Ananikov VP (2013) *Top Catal* 56:1246
- Kotha S, Lahiri K, Kashinath D (2002) *Tetrahedron* 58:9633
- Niakan M, Masteri-Farahani M (2022) *Tetrahedron* 108:132655
- Pai M, Ahmed E, Batakurki S, Kumar SG, Kusanur R (2023) *Appl Surf Sci Adv* 16:100427
- Kumar M, Sadaf I, Pamidighantam J, Anamika S, Kumar (2024) *J Heterocycl Chem* 61:29
- Gong L, Chen M, Tang Z, Chen Q, Zhang J, Hou G, Zhang J, Shen K, Liu Y, Tang Y (2023) *Surf Interfaces* 39:102867
- Lai CH, Lu MY, Chen LJ (2012) *J Mater Chem* 22:19
- Pearce CI, Patrick RAD, Vaughan DJ (2006) *Rev Mineral Geochem* 61:127
- Shiri L, Ghorbani-Choghamarani A, Kazemi M (2016) *Aust J Chem* 69:585
- Xiao Y, Lee SH, Sun YK (2017) *Adv Energy Mater* 7:1601329
- Dharmalingam P, Palani G, Apsari R, Kannan K, Lakkaboyana SK, Venkateswarlu K, Kumar V, Ali Y (2022) *Mater Today Sustain* 16:100232
- Dabiri M, Tavil HE, Lehi NF, Movahed SK, Salmasi AM, Souri S (2022) *J Phys Chem Solids* 162:110497
- Ong CL, Titinchi S, Juan JC, Khaligh NG (2021) *Helv Chim Acta* 104:e2100053
- Pramanik M, Choudhuri K, Mal P (2020) *Org Biomol Chem* 18:8771
- Kohzadian A, Filian H (2023) *SILICON* 15:4539
- Nikoorazm M, Ghorbani F, Ghorbani-Choghamarani A, Erfani Z (2018) *Appl Organomet Chem* 32:e4282
- Aphesteguy JC, Kurlyandskaya GV, de Celis JP, Safronov AP, Schegoleva NN (2015) *Mater Chem Phys* 161:243
- Almajidi YQ, Ubaidullah M, Panditc B, Kareemd AK, Romero-Parrae RM, Bobirjonf A, Kadhumg WR, AL-Erjanh AM, Abosoodai M, Mahmoudj AK (2023) *RSC Adv* 13:11393
- Barakat NAM, Kim B, Kim HY (2009) *J Phys Chem C* 113:531
- Nikoorazm M, Ghorbani-Choghamaranai A, Khanmoradi M, Moradi P (2018) *J Porous Mater* 25:1831
- Zare A, Kohzadian A, Abshirini Z, Sajadikhah SS, Phipps J, Benamara M, Beyzavi MH (2019) *New J Chem* 43:2247
- Esmailpour M, Sardarian AR, Javidi J (2014) *J Organomet Chem* 749:233
- Pires MJ, Purificacao SI, Santos AS, Marques MM (2017) *Synthesis* 49:2337
- Luo C, Zhang Y, Wang Y (2005) *J Mol Catal A: Chem* 229:7
- Briggs BD, Pekarek RT, Knecht MR (2014) *J Phys Chem C* 118:18543
- Peng YY, Liu J, Lei X, Yin Z (2010) *Green Chem* 12:1072
- Naghipour A, Fakhri A (2016) *Catal Commun* 73:39
- Ghorbani-Choghamarani A, Norouzi M (2016) *Appl Organometal Chem* 30:140
- Bai L, Wang JX (2007) *Adv Synth Catal* 350:315
- Samarasimharseddy M, Prabhu G, Vishwanatha TM, Sureshbabu VV (2013) *Synthesis* 45:1201
- Modak A, Mondal J, Sasidharan M, Bhaumik A (2011) *Green Chem* 13:1317
- Orgiu E, Crivillers N, Rotzler J, Mayor M, Samori P (2010) *J Mater Chem* 20:10798
- Emmanuvel L, Sudalai A (2007) *ARKIVOC* 14:126
- Nikoorazm M, Ghorbani-Choghamarani A, Noori N, Tahmasbi B (2016) *Appl Organometal Chem* 30:843
- Filian H, Ghorbani-Choghamarani A, Tahanpesar E (2019) *J Iran Chem Soc* 16:2673
- Ghorbani-Choghamarani A, Seydyosefi Z, Tahmasbi B (2018) *Appl Organomet Chem* 32:e4396
- Faria VW, Oliveira DGM, Kurz MHS, Gonçalves FF, Scheeren CW, Rosa GR (2014) *RSC Adv* 4:13446
- Rangraz Y, Nemati F, Elhampour A (2020) *J Phys Chem Solids* 138:109251
- Ghorbani-Choghamarani A, Taherinia Z (2016) *RSC Adv* 6:59410
- Zhao P, Yin H, Gao H, Xi C (2013) *J Org Chem* 78:5001

56. Veisi H, Zohrabi A, Karmakar SA, Karmakar B, Saremi SG, Varmira K, Hamelian M (2021) *J Organomet Chem* 951:122005
57. Rostami A, Rostami A, Ghaderi A (2015) *J Org Chem* 80:8694
58. Vibhute SP, Mhaldar PM, Shejwal RV, Pore DM (2020) *Tetrahedron Lett* 61:151594
59. Rostami A, Rostami A, Ghaderi A, Gholinejad M, Gheisarszadeh S (2017) *Synthesis* 49:5025
60. Yousofvand Z, Hajjami M, Ghorbani F, Ghafouri-Nejad R (2018) *J Porous Mater* 25:1349
61. Sabounchei SJ, Hashemi A (2014) *Inorg Chem Commun* 47:123
62. Nasrollahzadeh M, Azarian A, Maham M, Ehsani A (2015) *J Ind Eng Chem* 21:746
63. Singha S, Sahoo M, Parida KM (2011) *Dalton Trans* 40:7130

Publisher's Note Springer Nature remains neutral with regard to jurisdictional claims in published maps and institutional affiliations.

Springer Nature or its licensor (e.g. a society or other partner) holds exclusive rights to this article under a publishing agreement with the author(s) or other rightsholder(s); author self-archiving of the accepted manuscript version of this article is solely governed by the terms of such publishing agreement and applicable law.

Authors and Affiliations

Ebraheem Abdu Musad Saleh¹  · Asmaa F. Kassem^{1,2} · Farag M. A. Altalbawy^{3,4} · Sarah Jawad Shoja⁵ · Dmitry Olegovich Bokov^{6,7} · Ahmed Elawady^{9,10,8} · Ameer H. Al-Rubaye¹¹ · Abdunaser Saud¹² · Zuhair I. Al-Mashhadani¹³ · Maryam Sadat Ghorayshi Nejad¹⁴

✉ Maryam Sadat Ghorayshi Nejad
ghoreishinezhad2023@gmail.com;
mghoreishi1396@gmail.com

Ebraheem Abdu Musad Saleh
e.saleh@psau.edu.sa

Asmaa F. Kassem
a.kassem@psau.edu.sa

Farag M. A. Altalbawy
f_altalbawy@yahoo.com

Sarah Jawad Shoja
sarah.shoja@alayan.edu.iq

Dmitry Olegovich Bokov
bokov_d_o@staff.sechenov.ru

Ahmed Elawady
ahmedelawady85@gmail.com

Ameer H. Al-Rubaye
amir.hazim@uokitab.edu.iq

Abdunaser Saud
dr.abdunaser.s@huc.edu.iq

Zuhair I. Al-Mashhadani
zohair.al.path@nuc.edu.iq

¹ Department of Chemistry, College of Science and Humanities in Al-Kharj, Prince Sattam Bin Abdulaziz University, Al-Kharj 11942, Saudi Arabia

² Chemistry of Natural and Microbial Products Department, Pharmaceutical and Drug Industries Research Institute, National Research Centre, Dokki, Cairo 12622, Egypt

³ Department of Chemistry, University College of Duba, University of Tabuk, Tabuk, Saudi Arabia

⁴ National Institute of Laser Enhanced Sciences (NILES), University of Cairo, Giza 12613, Egypt

⁵ College of Health & Medical Technology, Al-Ayen University, Nasiriyah, Iraq

⁶ Institute of Pharmacy, Sechenov First Moscow State Medical University, 8 Trubetskaya St., bldg. 2, Moscow 119991, Russia

⁷ Laboratory of Food Chemistry, Federal Research Center of Nutrition, Biotechnology and Food Safety, 2/14 Ustyinsky pr, Moscow 109240, Russia

⁸ College of Technical Engineering, the Islamic University, Najaf, Iraq

⁹ College of Technical Engineering, the Islamic University of Al Diwaniyah, Al Diwaniyah, Iraq

¹⁰ College of Technical Engineering, the Islamic University of Babylon, Babylon, Iraq

¹¹ Department of Petroleum Engineering, Al-Kitab University, Altun Kupri, Iraq

¹² Department of Pharmacy, Al-Hadi University College, Baghdad 10011, Iraq

¹³ Department of Medical Engineering, Al-Nisour University College, Baghdad, Iraq

¹⁴ Takin Shimi Sepanta Industries Co, Sirvan Industrial Zone, PO 6958140120, Ilam, Iran